

Exchange-correlation functional challenges in modeling quaternary chalcogenidesRobert B. Wexler ¹, Gopalakrishnan Sai Gautam ¹, and Emily A. Carter ^{1,2}¹*Department of Mechanical and Aerospace Engineering, Princeton University, Princeton, New Jersey 08544-5263, USA*²*Office of the Chancellor and Department of Chemical and Biomolecular Engineering, University of California, Los Angeles, Los Angeles, California 90095, USA*

(Received 29 March 2020; revised 3 July 2020; accepted 14 July 2020; published 5 August 2020)

The development of next-generation quaternary chalcogenides, such as $\text{Cu}_2\text{ZnSnS}_4$ (CZTS) and $\text{Cu}_2\text{ZnGeS}_4$ (CZGS), for solar energy and thermoelectric applications hinges upon both careful experimentation and accurate quantum mechanical modeling. To address the latter, many have turned to density functional theory (DFT), which offers several choices for the approximate treatment of electron exchange and correlation (XC). Popular XC functionals include the Perdew–Burke–Ernzerhof (PBE) generalized gradient approximation (GGA) and the recently developed strongly constrained and appropriately normed (SCAN) meta-GGA. Extensions of DFT functionals, such as adding a Hubbard U correction and introducing a fraction of the Fock exchange (hybrid functionals), have been used widely to model systems containing $3d$ metal ions. However, no studies yet have compared comprehensively PBE(+ U) and SCAN(+ U) in the quality of their predictions of the bulk and defect thermodynamics of quaternary chalcogenides, which play a critical role in device fabrication and performance. Hence, here we calculate the (i) 0 K formation energies of bulk Ge compounds and (ii) neutral defect formation energies including charge-balanced (e.g., $\text{Cu}_{\text{Zn}} + \text{Zn}_{\text{Cu}}$) and charge-imbalanced (e.g., Cu_{Sn}) combinations of antisites and vacancies in CZTS and CZGS using the PBE, PBE + U , SCAN, SCAN + U , and the hybrid Heyd–Scuseria–Ernzerhof XC frameworks. We find that the formation energies of charge-imbalanced defects are more sensitive to the choice of the XC functional than those of charge-balanced defects, which can be explained by the differences in the extent of penalization of defect-generated delocalized electrons/holes by PBE, PBE + U , SCAN, and SCAN + U . Additionally, our results show that SCAN systematically underbinds Ge-containing compounds, thus highlighting the need for even further improvement of XC functionals. Based on our findings, we recommend the use of SCAN for modeling quaternary chalcogenides because its errors are systematic, and it has the firmest theoretical underpinning. Our work provides guidance for future modeling of quaternary chalcogenides.

DOI: [10.1103/PhysRevB.102.054101](https://doi.org/10.1103/PhysRevB.102.054101)**I. INTRODUCTION**

Quaternary chalcogenides, specifically $\text{Cu}_2\text{ZnSnS}_4$ (CZTS) and $\text{Cu}_2\text{ZnGeS}_4$ (CZGS), find application in a number of important technologies such as solar cells [1–5], photocatalysts [6–8], and thermoelectrics [9–11]. Optimization of their performance benefits from synergy between experimental synthesis and characterization, and computational interpretation and prediction. The latter is contingent upon accurate total energies, which enable calculations of the thermodynamic, electronic, and vibrational properties that govern device operation. These include standard formation enthalpies for determining bulk stability, defect formation energies for computing defect concentrations, defect transition levels for assessing the likelihood of carrier recombination in solar-cell absorbers, band structures for analyzing the electronic structure (e.g., the band gap), phonons for calculating the thermal conductivity of thermoelectrics, surface energies for evaluating polycrystallinity, etc.

Over the last 30 years, density functional theory (DFT) [12,13] has become the preferred method for total energy calculations in condensed matter and materials physics due to its quantum-mechanical accuracy [14–17] and computational

efficiency [18]. The accuracy of DFT calculations, however, rests upon their description of electron exchange and correlation (XC), which typically is incorporated using approximate local and semilocal energy functionals. The commonly used local-density approximation (LDA) and the semilocal generalized gradient approximation (GGA) functionals often fail to reproduce experimental band gaps of semiconductors (which is an excited-state property) [19–24], identify precise ground-state polymorphs [25–32], and predict formation enthalpies of compounds that are layered and/or contain transition metals [33–38]. Meta-GGAs mitigate errors in polymorph prediction and formation enthalpies by including higher-order gradients of the electron density and/or the kinetic energy density [39–42]. However, meta-GGAs also suffer from electron self-interaction error, similar to GGA and LDA [43–47]. On the other hand, mixing GGAs (or LDAs) with exact Fock exchange (thus generating hybrid functionals) can reduce such an error within GGA (LDA) but the evaluation of the exact exchange tends to be computationally intractable for all but single-point calculations of large systems (~ 100 atoms) and geometry relaxations of small systems (~ 10 atoms) [48–50]. The Hubbard U correction [51] provides a cheap alternative to hybrid functional calculations for improving the description of the electronic structure [52–54] and prediction of the

formation enthalpy [33,38,55,56] from semilocal (and meta-GGA) XC functionals. However, its results depend quite strongly on the choice of the effective on-site interaction parameter ($U_{\text{eff}} = U - J$, where U is the Coulomb repulsion and J is the exchange screening), which is dependent on the orbital being corrected, element, and system [57–59].

Here, we focus on the strongly constrained and appropriately normed (SCAN) meta-GGA [60] as it naturally extends the popular Perdew-Burke-Ernzerhof (PBE) GGA [61], obeys all 17 known XC constraints, and is, by construction, nearly exact for rare-gas atoms (Ne, Ar, Kr, and Xe) and jellium surfaces. As evidenced by recent studies, SCAN shows promise for predicting the crystal structure [62,63], thermodynamic stability [64,65], and catalytic activity [47] of solid materials; in spite of this, there has been limited use of SCAN for calculating defect formation energies in quaternary chalcogenides [66–68]. Also, SCAN has not yet been tested rigorously on Ge-containing binary, ternary, and quaternary compounds, which can influence the bulk and defect properties of CZGS.

Although SCAN has a better fundamental underpinning than PBE, SCAN still suffers from self-interaction errors (SIEs), especially in oxides containing $3d$ transition metals and $4f$ rare earths [47]. However, the magnitude of SIEs with SCAN is significantly lower than PBE, as highlighted by the lower U corrections required with SCAN than PBE to yield quantitatively accurate redox enthalpies and lattice constants, and qualitatively accurate polymorph preferences and band gaps [47,69]. Because of its novelty, understanding the performance of SCAN + U is still a work in progress. Hence, we are motivated to provide an evaluation of the SCAN + U framework for neutral defect calculations in quaternary chalcogenides in this work.

In addition to SCAN and SCAN + U , DFT calculations of Cu-Zn-Sn- and Cu-Zn-Ge-based chalcogenides commonly employ PBE [70–72], PBE + U [73–76], and the range-separated Heyd-Scuseria-Ernzerhof (HSE) hybrid XC functional [77–79]. The accuracy of these approaches, however, depends on the properties that are calculated. For example, both PBE and SCAN are good for bulk thermodynamics of Cu, Zn, and Sn sulfides whereas PBE + U is better than PBE or SCAN for band structures, especially in systems with highly correlated electrons. So far, PBE, PBE + U , SCAN, and HSE have been shown to predict similar defect formation energies for charge-compensated defects (e.g., $\text{Cu}_{\text{Zn}} + \text{Zn}_{\text{Cu}}$) [5,66–68,72,80–82], but there is no evidence yet of a similar agreement on charge-uncompensated defects (e.g., Cu_{Zn} and V_{Cu} , where V = vacancy). For nonmetallic band structures, the accuracy of HSE typically is in fair agreement with that of the GW approximation [83–87]; however, the extent of agreement depends strongly on the amount of exact exchange added. For example, the default HSE06 [88] can overpredict band gaps, especially in transition-metal oxides [89]. HSE also exhibits severe errors in describing bulk metallic phases, as should be expected because Hartree-Fock theory diverges for metals [90]. Notwithstanding this evidence, there remains no consensus on a general-purpose XC functional and no detailed comparisons of PBE, PBE + U , SCAN, SCAN + U , and HSE for such quaternary chalcogenide systems, which this paper aims to address.

Below, we first provide a detailed description of our computational methods and a primer on the crystal structures of CZTS and CZGS. Subsequently, we discuss the curious case of Ge underbinding with SCAN, followed by the XC functional dependence of defect formation energies. Finally, we offer rationale for the functional dependence and make some concluding remarks regarding the judicious selection of XC functionals for the study of quaternary chalcogenides.

II. METHODS

A. Density functional theory calculations

We calculated the bulk and defect formation energies using periodic plane-wave DFT [12,13] as implemented in the Vienna *Ab initio* Simulation Package (VASP) [91–94]. We treated the electron XC interactions using the PBE GGA [61], the SCAN meta-GGA [60], and the HSE06 [88] functionals. For PBE + U and SCAN + U calculations, we used the rotationally invariant Hubbard U correction developed by Dudarev *et al.* [95]. We employed U values fitted from electrostatically embedded metal-oxide clusters described within unrestricted Hartree-Fock (UHF) theory [96] for PBE + U calculations, namely 3.6, 4.5, and 4.8 eV for Cu $3d$, Zn $3d$, and Sn $4d$ orbitals, respectively. Since SCAN theoretically is a more accurate XC functional than PBE, it should include a more accurate description of the electron exchange and, therefore, require a lower U correction. Accordingly, we used $U_{\text{lower}}^{\text{SCAN}} = U_{\text{UHF}}^{\text{PBE}} - 2$ eV as a rule of thumb [47]. In addition, for a few defects, we tested $U_{\text{upper}}^{\text{SCAN}} = U_{\text{UHF}}^{\text{PBE}}$ as an upper limit. Note that we set the U for Ge $3d$ equal to that of Sn $4d$ in both PBE + U and SCAN + U calculations, because Ge and Sn reside in the same group of the Periodic Table and, as a result, their valence d electrons behave similarly. Hereafter, we simply denote $U_{\text{UHF}}^{\text{PBE}}$ as U .

We used the projector augmented-wave (PAW) method [97] and the PAW datasets generated at the PBE level recommended by the Materials Project [98] for Cu ($4s^1 3d^{10}$), Zn ($4s^2 3d^{10}$), Sn ($5s^2 4d^{10} 5p^2$), Ge ($4s^2 3d^{10} 4p^2$), and S ($3s^2 3p^4$). For Ge and Cu, we find that the inclusion of semicore $3d$ and $3p$ states, respectively, in their PAW datasets only slightly affects the formation energies of compounds containing them (≤ 0.015 eV/atom; see Tables S1-2 in the Supplemental Material (SM) [99] and Refs. [66] and [98,100–112] therein where Table S2 also reports the effect of Cu semicore $3p$ states on the kesterite to stannite reaction energy and Cu chemical potentials). We expanded the wave functions using a plane-wave basis set with a 520 eV kinetic energy cutoff and sampled 8 k points per 4 Å, which, for CZTS, corresponds to a $6 \times 6 \times 3$, Γ -point-centered k -point grid (see Figs. S1-2 in the SM for convergence tests [99]). Note that we adopted the “accurate” VASP precision mode for setting the coarse and fine fast-Fourier-transform grids and real-space projectors and did not use symmetry to reduce the sampling of the Brillouin zone.

We performed collinear spin-polarized DFT calculations with ferromagnetic initial spin configurations and find that all final configurations are nonmagnetic. To accelerate self-consistent field convergence, we applied 0.05 eV of Gaussian electronic smearing. For Brillouin-zone integration, we

used the automatic, Γ -point-centered k -mesh generation in VASP. For PBE and PBE + U calculations, we included van der Waals (vdW) interactions using the DFT-D2 method of Grimme [113] and for SCAN (and SCAN + U) calculations, we did not, consistent with our previous work [66–68,74–76]. Note that adding a vdW correction to SCAN, via the SCAN + rVV10 functional of Peng *et al.* [62], does not (i) alter the DFT-SCAN 0 K formation energy of GeS₂ (Table S3), (ii) affect polymorph preference in CZTS/CZGS (Table S4), and (iii) significantly change defect formation energies (Table S5) from SCAN's predictions in CZTS and CZGS. We modeled defects in CZTS and CZGS using a 128-atom $2 \times 2 \times 2$ supercell. We relaxed bulk and defect structures using the conjugate gradient algorithm. Ion positions, cell shape, and cell volume were allowed to change during relaxation for bulk structures, while only ion positions were allowed to change for defect structures with the cell shape and volume fixed to the corresponding relaxed defect-free bulk structures. Finally, we set total energy convergence and force convergence thresholds of 10^{-5} eV/cell and 0.03 eV/Å, respectively. All of our defect calculations are neutral, i.e., we add (remove) all electrons of the ion added (removed) to create a given defect and did not include any compensating background charge. This is a drawback of our investigation because a considerable amount of work has shown that, in addition to neutral defects, charged defects greatly influence the photovoltaic properties of chalcogenides [114–118]. We previously studied charged defects in Cd- and Ag-doped CZTS and observed that qualitative trends with respect to changes in defect concentrations did not change from those observed with neutral defects but we did obtain important insights into carrier lifetimes [66]. Therefore, additional studies will be needed to benchmark the performance of different XC functionals for the wide range of charged defects that can form in CZTS and CZGS. The SM [99] contains additional details regarding the convergence of defect formation energies with respect to supercell size (Table S6) and the defect configurations (Fig. S3).

B. *Ab initio* thermodynamics

We used PYMATGEN [109] to calculate 0 K formation energies of bulk compounds, chemical potentials for different equilibria, and 0 K neutral defect formation energies. Here, we define 0 K formation energies as

$$\Delta E_f^{0K} = E_{\text{product}} - \sum_i^{\text{species}} n_i E_i \quad (1)$$

where i is an index that runs over the standard states of the species comprising the *product*, n_i is the stoichiometric coefficient of species i , and E_i is the DFT total energy per formula unit of species i . As for different equilibria, we focus on the experimentally relevant Cu-poor condition [5,66] where CZTS/CZGS are in equilibrium with S, SnS₂/GeS₂, and ZnS. To determine the chemical potentials (μ) of Cu, Zn, Sn/Ge, and S for these conditions, we use Eqs. (2a)–(2d) as chemical constraints:

$$\begin{aligned} 2\mu_{\text{Cu}} + \mu_{\text{Zn}} + \mu_{\text{Sn/Ge}} + 4\mu_{\text{S}} \\ = \Delta E_f^{0K} [\text{Cu}_2\text{ZnSnS}_4/\text{Cu}_2\text{ZnGeS}_4] \end{aligned} \quad (2a)$$

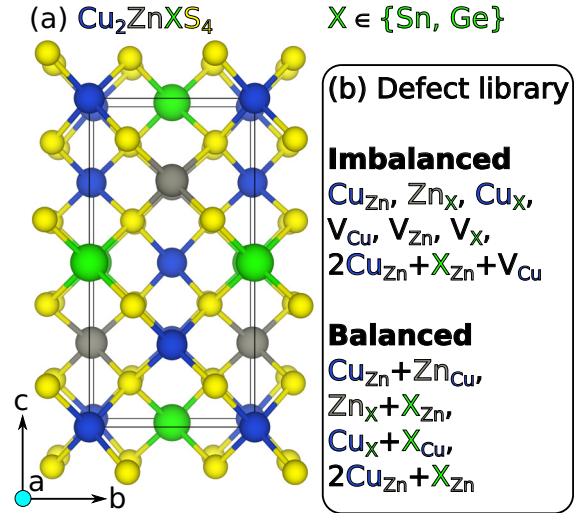


FIG. 1. (a) Crystal structure of kesterite Cu_2ZnXS_4 where X is either Sn or Ge. Blue, gray, green, and yellow balls correspond to Cu, Zn, X (Sn/Ge), and S, respectively. See Fig. S4 in the SM [99] for the crystal structures of stannite and wurtzite Cu_2ZnXS_4 . (b) A list of charge-imbalanced and charge-balanced neutral defects we considered in this study.

$$\mu_{\text{S}} = \Delta E_f^{0K} [\text{S}] \equiv 0 \quad (2b)$$

$$\mu_{\text{Sn/Ge}} + 2\mu_{\text{S}} = \mu_{\text{Sn}} = \Delta E_f^{0K} [\text{SnS}_2/\text{GeS}_2] \quad (2c)$$

$$\mu_{\text{Zn}} + \mu_{\text{S}} = \mu_{\text{Zn}} = \Delta E_f^{0K} [\text{ZnS}] \quad (2d)$$

where the ΔE_f^{0K} s of Ge-containing compounds include a correction term (see below). We define 0 K neutral defect formation energies as

$$\Delta E_f^d = E_{\text{defect}} - E_{\text{bulk}} + \sum_i^{\text{species}} n_i \mu_i \quad (3)$$

where n_i is the number of species i added (< 0) and/or removed (> 0), respectively, as a result of defect formation. The SM [99] contains 0 K formation energies for binary, ternary, and quaternary compounds containing Cu, Zn, Sn, Ge, and S (Table S3), as well as chemical potentials of each species for different equilibria (Table S7).

C. CZTS and CZGS crystal structures and choice of defects

Both CZTS and CZGS crystallize in the $I\bar{4}$ space group of the mineral kesterite, which has a body-centered Bravais lattice and a fourfold improper rotation-reflection axis. While this is the stable form of CZTS and CZGS, they also exist in the $I\bar{4}2m$ and $Pmn2_1$ space groups of the minerals stannite and wurtzite, respectively (see Fig. S4 in the SM [99] for the crystal structures of these polymorphs). Figure 1(a) shows the 16-atom conventional cell of kesterite CZTS and CZGS. Each cation (Cu^{1+} , Zn^{2+} , Sn^{4+} , and Ge^{4+}) forms a tetrahedral coordination environment with four S^{2-} . Along the \mathbf{c} -lattice vector, the cation composition alternates between $\text{Cu} + \text{X}$ and $\text{Cu} + \text{Zn}$ where X is either Sn or Ge.

Defects play an important role in the performance of solar-cell absorbers, thermoelectrics, and photocatalysts. For example, the efficiency deficit in CZTS-based solar cells was suggested recently to be due to the formation of $2\text{Cu}_{\text{Zn}} + \text{Sn}_{\text{Zn}}$ defect clusters, which induces deep-trap states and therefore promotes carrier recombination [68,82,119,120]. On the other hand, the formation of the Cu_{Zn} defect in CZXS ($X = \text{Sn}, \text{Ge}$) has been used to tune its electrical and thermal conductivity for thermoelectric applications [9,71] and photocatalytic activity for water splitting [7,121]. Here, we evaluate the XC functional dependence on the calculated formation energies of the aforementioned clusters in CZTS and CZGS, and also include a few other defect clusters for completeness.

Figure 1(b) presents the neutral defect library we consider, in a notation similar to Kröger-Vink [122], which follows the scheme M_S where M is the species (e.g., an atom, vacancy, interstitial, electron, hole, etc.) and S is the lattice site that M occupies. The library lists both charge-imbalanced and -balanced defects. For example, Cu_{Zn} is a charge-imbalanced (CI) defect because it generates a hole (h^+) to preserve charge neutrality



where $'$ means a negative charge. However, we only refer to this defect as Cu_{Zn} , which implicitly is balanced with a hole. Conversely, $\text{Cu}_{\text{Zn}} + \text{Zn}_{\text{Cu}}$ is a charge-balanced (CB) defect because it does not generate charge carriers—the excess h^+ of Cu_{Zn} is compensated by the excess e^- of Zn_{Cu} . For CI defects, our library includes antisites, vacancies, and antisite-vacancy clusters whereas for CB defects, it only includes antisite clusters.

III. RESULTS

A. Systematic underbinding of Ge-containing compounds by SCAN

For Cu, Zn, and Sn sulfides, we previously demonstrated that SCAN reproduces experimental formation enthalpies within a ± 0.1 eV accuracy, better than PBE [66]. However, such benchmarking has not been performed rigorously across binary Ge compounds. The accuracy of SCAN/PBE in describing the formation enthalpies of the binary Ge sulfides and Cu-Ge intermetallics will be crucial in determining the Ge chemical potential, which in turn determines defect formation energies in CZGS and analogous compounds.

In the first part of this study, we assess SCAN's ability to reproduce the experimental standard formation enthalpies ($\Delta H_f^{298\text{K}}$) of the following Ge-containing compounds: Cu_3Ge , GeS , GeS_2 , Ge_3N_4 , GeF_2 , GeO_2 , GeP , GeI_2 , GeI_4 , GeSe , GeSe_2 , GeTe , Mg_2Ge , MgGeO_3 , and Ni_2Ge . These compounds span binary intermetallics (Cu_3Ge , Mg_2Ge , and Ni_2Ge), pnictides (Ge_3N_4 and GeP), chalcogenides (GeO_2 , GeS , GeS_2 , GeSe , GeSe_2 , and GeTe), halides (GeF_2 , GeI_2 , and GeI_4), and ternaries (MgGeO_3), thus representing a rigorous test for SCAN's accuracy and range of applicability. Note that, while we compare $\Delta E_f^{0\text{K}}$ to $\Delta H_f^{298\text{K}}$, these quantities are, in principle, not equal. In fact, $\Delta E_f^{0\text{K}}$ is just one of four

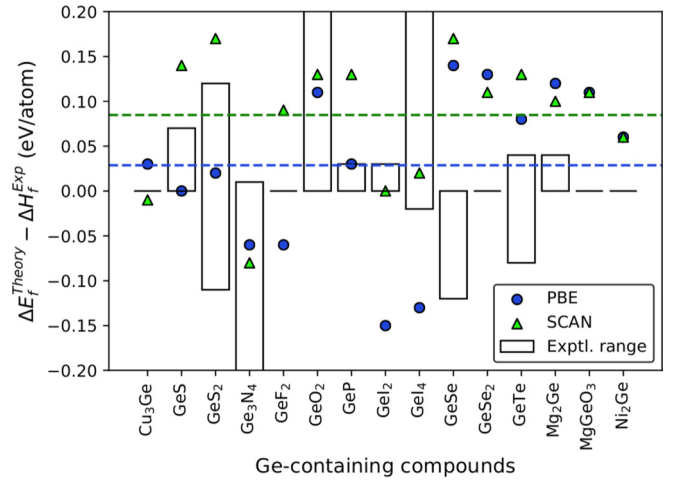


FIG. 2. Errors in DFT formation energies compared to experiment for a series of Ge-containing compounds. PBE 0 K formation energies are taken from The Open Quantum Materials Database (OQMD) [124]. Black rectangles correspond to the range of experimental standard (298 K) formation enthalpies. Blue (green) dashed line corresponds to the mean signed deviation (MSD, i.e., mean of $\Delta E_f^{\text{Theory}} - \Delta H_f^{\text{Exp}}$) using PBE (SCAN). For a discussion of the quality of this experimental thermochemical data, please see the caption for Table S3 in the SM [99].

contributions to $\Delta H_f^{298\text{K}}$,

$$\Delta H_f^{298\text{K}} = \Delta E_f^{0\text{K}} + \Delta \text{ZPE} + \Delta(\text{IHC}) + \Delta(pV) \quad (5)$$

where ZPE is the zero-point energy, IHC is the integrated isobaric heat capacity from 0 to 298 K, p is the pressure, and V is the volume. For the formation of solid compounds from solid standard-states, the last three terms in Eq. (5) are negligible, e.g., $\Delta(pV) \approx 2 \times 10^{-6}$ eV/atom [123]; hence, $\Delta H_f^{298\text{K}} \approx \Delta E_f^{0\text{K}}$.

Figure 2 shows the difference between theoretical 0 K formation energies ($\Delta E_f^{\text{Theory}}$) and experimental (Exp) standard formation enthalpies (ΔH_f^{Exp}) for all Ge-containing compounds with experimental data. Positive and negative values on the vertical axis correspond to the underbinding and overbinding, respectively, with respect to experimental values reported in Ref. [110]. We report PBE (blue circles) and SCAN (green triangles) differences for each compound, as well as the experimental range (black-outlined bars and rectangles). The absence of a bar indicates either that there is only one experimental value or that all values are the same. The bottom and top of the rectangles correspond to the minimum and maximum experimental values, respectively, also relative to that of Ref. [110] (see Table S3 in the SM [99] for additional details regarding experimental data).

Our results show that PBE overbinds Ge_3N_4 and the halides (GeF_2 , GeI_2 , and GeI_4) and underbinds most of the chalcogenides (GeO_2 , GeSe , GeSe_2 , and GeTe), two of three intermetallics (Mg_2Ge and Ni_2Ge), and MgGeO_3 . With that being said, PBE does make accurate predictions (i.e., $|\Delta E_f^{\text{Theory}} - \Delta H_f^{\text{Exp}}| \leq 0.05$ eV/atom) for Cu_3Ge , GeS , GeS_2 , and GeP . For PBE, the mean absolute error (MAE) and mean signed deviation (MSD, dashed blue line) are

0.27 ± 0.20 eV/Ge and 0.10 ± 0.32 eV/Ge, respectively. Note that the PBE MSD plotted in Fig. 2 is in units of eV/atom – hence, an MSD of 0.10 eV/Ge in GeO_2 is equivalent to ~ 0.03 eV/atom. The MAE and MSD of PBE indicate that while PBE deviates from experiment, it does so nonsystematically (scattered about the 0 eV line). In contrast, SCAN overbinds only Ge_3N_4 and underbinds the chalcogenides (GeO_2 , GeS , GeS_2 , GeSe , GeSe_2 , and GeTe), the same intermetallics as PBE (Mg_2Ge and Ni_2Ge), GeF_2 , GeP , and MgGeO_3 . SCAN gives accurate predictions for Cu_3Ge and the iodides (GeI_2 and GeI_4). The MAE for SCAN (0.27 ± 0.16 eV/Ge) is equal to that of PBE, demonstrating that both XC functionals deviate similarly from experiment. The MSD for SCAN (0.27 ± 0.17 eV/Ge, dashed green line in Fig. 2), however, is the same as its MAE, suggesting that SCAN's errors are systematic. So, while SCAN is, on average, less accurate ($\text{MSD} = 0.27$ eV/Ge) than PBE (0.10 eV/Ge), it is also more precise (standard deviation of $\text{MSD} = 0.17$ eV/Ge for SCAN and 0.32 eV/Ge for PBE). Thus, by subtracting 0.27 eV/Ge from all SCAN formation energies of Ge-containing compounds, we obtain formation energies that are in better agreement with experiment than those of either PBE or SCAN and are equally precise as those of SCAN. Subsequently, we use the Ge-corrected SCAN energies in Eq. (2) to determine Cu-poor chemical potentials for defect formation energy calculations. One should be careful in using this correction when bonds between Ge and Cu, N, or I are present; however, this is not the case for CZTS nor CZGS and therefore this correction should provide more accurate chemical potentials and defect formation energies than either PBE or SCAN.

B. XC functional dependence of defect formation energies

In this section, we compare CZTS and CZGS ΔE_f^d [Eq. (3)] for the following XC functionals: PBE, PBE + U , SCAN, SCAN + ($U - 2$), SCAN + U , and HSE. We consider the CI and CB defects listed in Fig. 1(b). For CI defects, we examine antisites, vacancies, and antisite-vacancy clusters that generate one h^+ (Cu_{Zn} , V_{Cu} , and $2\text{Cu}_{\text{Zn}} + \text{X}_{\text{Zn}} + \text{V}_{\text{Cu}}$ where $X = \text{Sn}$ or Ge in what follows), two h^+ (Zn_X and V_{Zn}), three h^+ (X_{Cu}), and four h^+ (V_X) to understand the relationship between CI and the agreement between XC functionals. For CB defects, we study charge-compensated antisite clusters such as $\text{Cu}_{\text{Zn}} + \text{Zn}_{\text{Cu}}$ ($1h^+ + 1e^-$), $\text{Zn}_X + \text{X}_{\text{Zn}}$ ($2h^+ + 2e^-$), $\text{Cu}_X + \text{X}_{\text{Cu}}$ ($3h^+ + 3e^-$), and $2\text{Cu}_{\text{Zn}} + \text{X}_{\text{Zn}}$ (also $2h^+ + 2e^-$). While these charge carriers compensate each other, there remains localized CI on the defect sites. For example, for $\text{Cu}_{\text{Zn}} + \text{Zn}_{\text{Cu}}$, the h^+ and e^- localize on the Cu_{Zn} and Zn_{Cu} antisites, respectively (see Fig. 4 and discussion below). Consequently, these defects probe the more subtle correlation between local CI and XC functionals.

Figure 3 shows the formation energies for all defects in CZTS (panels a, b) and CZGS (panels c, d) at the Cu-poor synthesis condition, which is relevant for solar-cell fabrication. For all defects, either PBE (blue bars) or SCAN (green bars) predicts the lowest ΔE_f^d whereas PBE + U (gray bars) and HSE (white bars) constitute the upper bound. Note that for defects, other than $\text{Cu}_{\text{Zn}} + \text{Zn}_{\text{Cu}}$, with both HSE and PBE + U ΔE_f^d , we find the HSE ΔE_f^d to be slightly larger than those of PBE + U . Since GGAs tend to overdelocalize

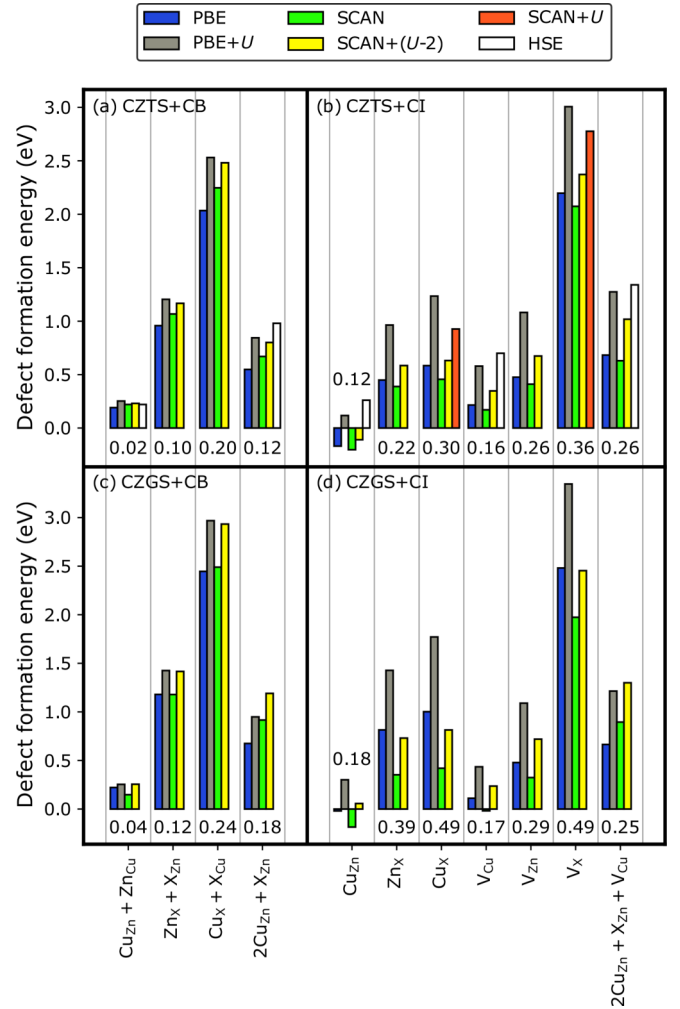


FIG. 3. XC functional dependence of neutral defect formation energies in (a), (b) $\text{Cu}_2\text{ZnSnS}_4$ and (c), (d) $\text{Cu}_2\text{ZnGeS}_4$. Includes both charge-imbalanced (e.g., Cu_{Zn} generates a hole) and charge-balanced (e.g., $\text{Cu}_{\text{Zn}} + \text{Zn}_{\text{Cu}}$ generates a hole and an electron) defects. Numbers above or below the bars correspond to the standard deviation (eV) of the defect formation energies calculated using PBE, PBE + U , SCAN, and SCAN + ($U - 2$). The black vertical line between $2\text{Cu}_{\text{Zn}} + \text{X}_{\text{Zn}}$ and Cu_{Zn} separates CB (a), (c) from CI (b), (d) defects. Gray grid lines separate individual defects.

electrons and the addition of U or exact exchange attempts to correct this, the true ΔE_f^d likely lies between these bounds. Also, given that SCAN describes XC better than PBE, and we employ a smaller absolute U correction ($U - 2$ eV), SCAN + ($U - 2$)'s ΔE_f^d predictions (yellow bars) are consistently lower than PBE + U and higher than PBE/SCAN in both CZTS and CZGS. Importantly, our results show that CB defects ($\text{Cu}_{\text{Zn}} + \text{Zn}_{\text{Cu}}$, $\text{Zn}_X + \text{X}_{\text{Zn}}$, $\text{Cu}_X + \text{X}_{\text{Cu}}$, and $2\text{Cu}_{\text{Zn}} + \text{X}_{\text{Zn}}$) generally produce smaller XC functional variations (see $\sigma_{\Delta E_f^d}$ either above or below bars) than CI defects (Cu_{Zn} , Zn_X , Cu_X , V_{Cu} , V_{Zn} , V_{Sn} , and $2\text{Cu}_{\text{Zn}} + \text{X}_{\text{Zn}} + \text{V}_{\text{Cu}}$). In other words, the greater the overall CI, the greater the XC functional variations; we will analyze this relationship in the subsequent section.

Interestingly, SCAN stabilizes metal vacancies compared to PBE, as indicated by the lower ΔE_f^d predicted for V_{Cu} , V_{Zn} ,

and V_X in Cu_2ZnXS_4 ($X = \text{Sn, Ge}$). We rationalize this on the basis that SCAN ($\Delta E_f^{\text{SCAN}} = -0.54$ eV/atom) underbinds CZTS compared to PBE ($\Delta E_f^{\text{PBE}} = -0.63$ eV/atom), which makes it easier for CZTS to form vacancies, with the same explanation applying to CZGS. Despite these differences in CZTS and CZGS binding, polymorph preference (kesterite vs stannite vs wurtzite) is functional insensitive (see Table S4 in the SM [99] for additional details).

Surprisingly, Cu_{Zn} is predicted to form spontaneously ($\Delta E_f^d < 0$, Fig. 3) in CZTS for PBE, SCAN, and SCAN + ($U - 2$) and CZGS for PBE and SCAN. PBE + U and HSE (and SCAN + ($U - 2$) for CZGS), on the other hand, predict nonspontaneous Cu_{Zn} formation ($\Delta E_f^d > 0$), which is more sensible considering CZTS and CZGS are known to be stable experimentally. This issue for PBE and SCAN stems from the fact that both functionals overestimate the spontaneity of Cu oxidation from a 1+ to a 2+ oxidation state. Take, for example, the oxidation of $\text{Cu(I)}_2\text{S}$ to Cu(II)S :



Since we have shown that there are no SCAN errors from S [66], any theory error in Eq. (6) is coming from $\text{Cu(I)} \rightarrow \text{Cu(II)}$, which is an oxidation reaction. Compared to the -0.26 eV per S atom experimental oxidation enthalpy [110], PBE and SCAN yield overly spontaneous oxidation (-0.51 and -0.52 eV/S, respectively). Only a $U = 3.5$ to 4 eV corrects PBE and obtains a more physically reasonable result [33], while applying a U correction to SCAN has yielded mixed results in Cu oxides [69].

We further analyze the effect of U corrections on PBE and SCAN ΔE_f^d for Cu_{Sn} and V_{Sn} , as they exhibit the largest CI and XC variability for CZTS. We find that U increases the PBE ΔE_f^d (PBE + U - PBE = 0.65 eV for Cu_{Sn} and 0.81 eV for V_{Sn}) more than those calculated using SCAN (SCAN + U - SCAN = 0.47 eV for Cu_{Sn} and 0.70 eV for V_{Sn}), which is consistent with the intuition that SCAN treats XC better than PBE and is therefore less affected by U corrections. As a final point, while some defects suffer from large XC variability, the qualitative trends in ΔE_f^d are mostly functional insensitive (see Fig. S5 in SM [99] for additional details). For example, V_{Zn} exhibits a higher ΔE_f^d in both CZTS and CZGS compared to V_{Cu} , irrespective of which XC functional is used.

C. Global vs local charge imbalance in CZTS

In the preceding section, we point out that XC functional agreement depends on the nature of the defect-induced CI, i.e., the number of charge carriers it generates and their spatial localization. We now will explore this further in CZTS, the more widely studied material among CZTS and CZGS, for the following three different types of defects: (1) antisites (Cu_{Zn} , Zn_{Sn} , and Cu_{Sn}), (2) vacancies (V_{Cu} , V_{Zn} , and V_{Sn}), and (3) antisite clusters ($\text{Cu}_{\text{Zn}} + \text{Zn}_{\text{Cu}}$, $\text{Zn}_{\text{Sn}} + \text{Sn}_{\text{Zn}}$, and $\text{Cu}_{\text{Sn}} + \text{Sn}_{\text{Cu}}$). The first two types are globally CI or simply CI in the sense that they generate compensating charge carriers. In contrast, the third type is locally CI because even as they produce compensating charge carriers on each defect site, the defect pairs produce equal numbers of complementary carriers, thus globally CB or simply CB. In addition to a diversity in CI, we vary within each defect type the magnitude

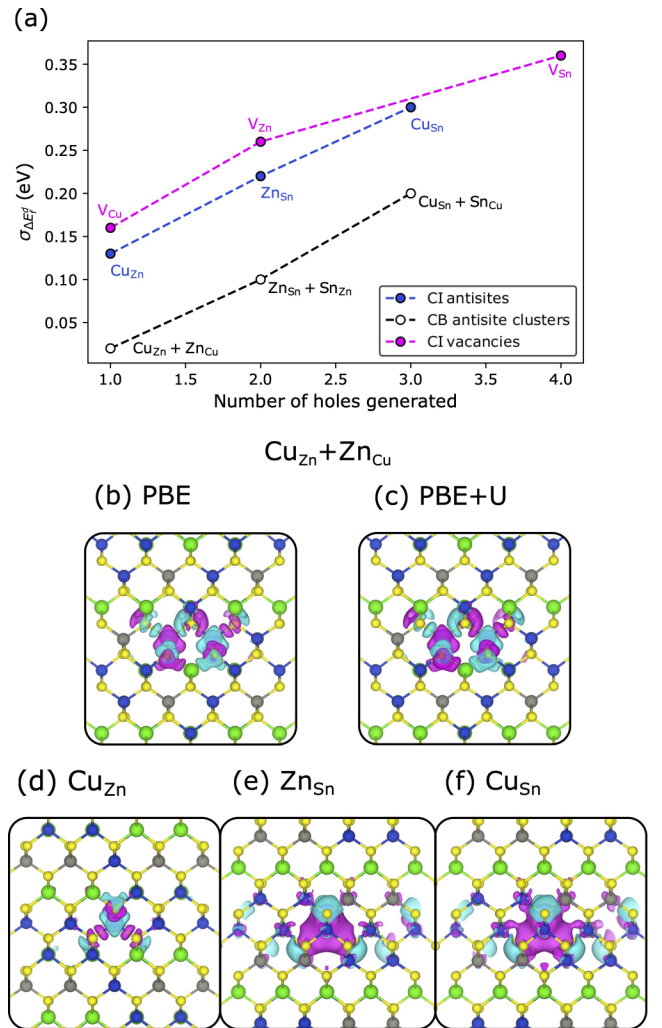


FIG. 4. (a) Effect of the number of defect-generated charge carriers on the agreement between different XC functionals for $\text{Cu}_2\text{ZnSnS}_4$. For a given defect, this agreement is measured by the SD of its formation energy. Blue/magenta and gray data points correspond to CI and CB defects, respectively. (b) PBE and (c) PBE + U electron density difference plots ($|\text{isosurface}| = 0.001$ e/bohr³) showing the relative localization of holes and electrons in the CB antisite cluster $\text{Cu}_{\text{Zn}} + \text{Zn}_{\text{Cu}}$. (d)–(f) PBE electron density difference plots ($|\text{isosurface}| = 0.001$ e/bohr³) showing the relative localization of electrons and holes in CI antisites. Cyan and magenta regions correspond to electron and hole accumulation, respectively.

of the CI. For example, for the first type (i.e., CI antisites), we survey Cu_{Zn} , Zn_{Sn} , and Cu_{Sn} , which generate $1h^+$, $2h^+$, and $3h^+$, respectively.

Figure 4(a) shows the standard deviation (SD) of the ΔE_f^d in Figs. 3(a) and 3(b) as a function of the number of h^+ generated by the neutral defect. This SD is a measure of the variation/agreement between XC functionals where smaller and larger values correspond to better and worse agreement, respectively. We report SDs for CI antisites (blue circles), CB antisite clusters (white circles), and CI vacancies (magenta circles). Our results indicate that the SD increases with the number of h^+ generated. Also, the SD is higher for CI defects compared to CB defects that generate the same number of

h^+ globally or locally. For example, the SD of the CI Cu_{Sn} antisite is higher (0.30 eV) than that of the CB $\text{Cu}_{\text{Sn}} + \text{Sn}_{\text{Cu}}$ (0.20 eV) despite both defects generating $3h^+$. Additionally, SDs for vacancies are larger than CI antisites, which can be attributed to two factors: (i) CIs being accommodated by changes in the oxidation state(s) of cation(s) that constitute the antisites, while the CI in vacancies typically lead to excess carrier generation, and (ii) accuracy of the XC functional in describing the excess carriers and/or cation oxidation state changes.

Figures 4(b) and 4(c) show that the PBE and PBE + U electron density differences for $\text{Cu}_{\text{Zn}} + \text{Zn}_{\text{Cu}}$, a CB defect, are similar in both size and shape. This demonstrates that + U only makes minute changes in the electron density and, therefore, the difference between the PBE and PBE + U formation energies of CB defects can be attributed to the + U energy penalty. Figures 4(d)–4(f) then show that, for CI antisites, generated charge-carrier delocalization increases with increasing (local and global) CI. As a result, the + U energy penalty also increases with increasing CI. Analogously, one can think of the action of + U on PBE and SCAN not as redistributing electron density in CZTS but rather as energetically penalizing delocalization. Hence, as charge delocalization increases (with increasing CI), PBE + U and SCAN + ($U - 2$) increasingly predict higher increases in ΔE_f^d compared to the corresponding PBE and SCAN values, leading to an increase in the SD across functionals [see positive correlation between SD and number of h^+ in Fig 4(a)]. For CI defects, differences in how strongly the functionals bind the reservoir phases (ZnS , SnS_2 , SnS , and S) can also affect the SD; however, this effect is difficult to quantify for PBE + U and SCAN + U because they cannot be used, in a theoretically justified manner, to calculate the formation energies of metal-containing reservoir phases with respect to their standard states. As an aside, the differences between the PBE and SCAN defect formation energies, for both CI and CB defects, are small, with SCAN in most cases giving the lower bound—this is due to (i) small electron density differences between PBE and SCAN that are difficult to detect visually and (ii) the weaker binding of CZTS by SCAN.

IV. DISCUSSION

In the first part of this study, we report that SCAN systematically underbinds Ge-containing compounds (Fig. 2), which, in turn, leads to the not negative enough prediction of μ_{Ge} for different equilibria (see Table S7 in the SM [99]). This systematic trend indicates that Ge, and not the other species, causes the errors. To complicate matters further, SCAN correctly selects the cubic diamond polymorph of Ge as the ground state and accurately predicts the pressure of its phase transition to the β -Sn crystal structure ($p^{\text{Theory}} = 10.9$ GPa vs $p^{\text{Exp}} = 11.3 - 12.6$ GPa [125]). Altogether, the performance of SCAN for Ge and its compounds is, at best, enigmatic. There are two possible routes to improve SCAN and avoid *ad hoc* Ge corrections: (1) generate SCAN PAW datasets as, to the best of our knowledge, they do not exist yet (here PBE PAW data sets are employed, which introduces an inconsistency) and (2) refine SCAN by adding more appropri-

ate norms (e.g., spin-polarized systems) [126]. Implementing these solutions, however, goes beyond the scope of this work.

Next, we compare the quality of SCAN to other XC functionals. We find that they are quantitatively consistent for CB antisite clusters ($\text{Cu}_{\text{Zn}} + \text{Zn}_{\text{Cu}}$, $\text{Zn}_X + \text{X}_{\text{Zn}}$, $\text{Cu}_X + \text{X}_{\text{Cu}}$, and $2\text{Cu}_{\text{Zn}} + \text{X}_{\text{Zn}}$) and qualitatively consistent for CI antisites (Cu_{Zn} , Zn_X , and Cu_X), vacancies (V_{Cu} , V_{Zn} , and V_X), and their clusters ($2\text{Cu}_{\text{Zn}} + \text{X}_{\text{Zn}} + \text{V}_{\text{Cu}}$). This poor quantitative agreement for CI defects emanates from differences in how XC functionals penalizes electron delocalization. We also learn that SCAN, for most defects, provides a lower limit for their formation energies (i.e., a worst-case scenario for defect formation). In other words, that SCAN predicts defects to be more abundant than DFT + U or HSE. However, since relative trends in defect formation energies are consistent, SCAN (or PBE) can answer questions such as, “Does ion substitution promote/suppress defect formation?,” but not, “By how much?,” an issue that still is prevalent in defect literature [106].

To reduce the quantitative error in estimating defect formation energies, we must identify the “best” XC functional for accurate and efficient modeling of quaternary chalcogenides. To this end, it is important for the field to have comprehensive XC benchmarking. This paper is but a first step, as many other cationic (Ag^{1+} , Cd^{2+} , Na^{1+} , K^{1+} , Mg^{2+} , Si^{4+} , etc.) [66,80,127,128] and anionic (Se^{2-}) [129] substituents have been proposed in the literature, each requiring benchmark calculations of ΔE_f^{OK} , μ , and ΔE_f^d . XC benchmarking, however, starts with better/more experimental thermochemistry data. For example, Fig. 2 shows that the range of ΔH_f^{Exp} for GeS_2 , Ge_3N_4 , GeO_2 , and GeI_4 exceeds 0.2 eV/atom, beyond errors that are typical (<0.1 eV/atom) across measurements. Hence, it is critical to revisit these measurements and obtain data that are better curated. Moreover, despite the technological relevance of CZTS and CZGS, the literature does not contain measurements of their $\Delta H_f^{298\text{K}}$. Thus, we urge the experimental community to carry out these measurements as they will enable more reliable and insightful interpretations of subsequent experiments. It also would be beneficial to have measurements of defect concentrations (e.g., quantify the concentration of deep traps and/or the extent of Cu-Zn disorder) to validate theoretical predictions.

Answering “by how much does ion substitution promote/suppress defect formation?” also requires theoretical method development. In particular, we need U_{UHF} values for Ge as well as other common dopants in CZTS, preferably based on sulfide, and not oxide, clusters. As a general rule, PBE/SCAN and PBE + U / HSE provide lower and upper limits for defect formation energies, respectively, with SCAN being as computationally expensive as PBE/PBE + U calculations. Because we find that the ground-state electron density is functional insensitive, it is likely that the ground-state structure is, as well. In case there is interest in benchmarking non-HSE hybrid functional predictions, a computationally minimally invasive procedure would be to perform self-consistent field calculations, with input geometries and electron densities from PBE/SCAN. Unfortunately, however, hybrid functionals are problematic when considering Cu-rich conditions (metallic Cu in equilibrium with CZTS [66]) because they overlocalize the Cu $3d$ electrons [130,131].

TABLE I. XC functional dependence of the CZTS and CZGS band (eigenvalue) gap. Kohn-Sham gaps [132,133] are derived from band-structure calculations, which are displayed in Figs. 6–9 in the SM [99].

XC	Band gap (eV)	
	CZTS	CZGS
PBE	0.21	0.71
PBE + U	0.93	1.51
SCAN	0.02	0.39
SCAN + rVV10	0.02	0.40
SCAN + ($U-2$)	0.21	0.79
SCAN + U	0.60	1.22
HSE	1.31, 1.49 [77]	2.07 [134]
Exp.	1.39–1.52 [135]	2.10 [11]

Next, we attempt to develop a physical intuition for the functional-sensitivity of ΔE_f^d for CB and CI defects. Take, for example, the simplest CB defect in this study, $\text{Cu}_{\text{Zn}} + \text{Zn}_{\text{Cu}}$. At the hypothetical moment of defect formation, Cu_{Zn} and Zn_{Cu} generate $1h^+$ and $1e^-$ localized on Cu and Zn, respectively. These charge carriers neighbor each other in the minimum energy defect configuration, i.e., both Cu_{Zn} and Zn_{Cu} in the Cu + Zn plane. This proximity stabilizes the $e^- - h^+$ pair via electrostatics, thus reinforcing its spatial localization and reducing the effect of XC functional delocalization penalty on ΔE_f^d . Now consider the CI antisite, $\text{Zn}_{\text{Sn/Ge}}$, which produces $2h^+$. Unlike the $e^- - h^+$ pair, these $2h^+$ experience electrostatic repulsion, which causes their delocalization. This delocalization explains the observed dependence of ΔE_f^d on U for CI defects, i.e.,

$$\text{SCAN} \lesssim \text{PBE} < \text{SCAN} + (U - 2) < \text{PBE} + U, \quad (7)$$

where ΔE_f^d increases from left to right. Equation (7) also shows that SCAN ΔE_f^d for CI defects are lower than those for PBE (except for $2\text{Cu}_{\text{Zn}} + \text{Ge}_{\text{Zn}} + \text{V}_{\text{Cu}}$).

Due to the potential influence of charged defects on the performance of CZTS-based solar cells and the role of the band gap/edges in determining the character of the charged-defect induced gap states (i.e., whether they will act as electron donors/acceptors or traps that assist electron-hole recombination) [66,82,136–139], we analyze the dependence of the CZTS and CZGS band (eigenvalue) gaps on the choice of XC functional (Table I). First, we see that all XC functionals considered capture the experimentally observed increase in the band gap going from CZTS to CZGS. PBE and SCAN also reproduce the direct band gap of both materials, as shown in Figs. S6-9 in the SM [99]. As expected, the semilocal XC functionals PBE and SCAN, both with and without U - and/or

vdW-corrections, underestimate the experimental band gaps considerably. That being said, the application of U corrections predictably increases the band gaps. Given that SCAN is perceived to be superior to most other gradient-corrected, semilocal XC functionals [140], it is surprising that SCAN and SCAN + U predict smaller band gaps than PBE and PBE + U , respectively, for both CZTS and CZGS. However, this appears to be a more general trend, as observed in $3d$ transition-metal and rare-earth oxides [47,69]. The lower band gaps predicted by SCAN are also a factor in the consistently lower defect formation energies predicted by SCAN versus the other functionals considered here. Consequently, further research is needed to better understand the source of this counterintuitive behavior for SCAN band-gap predictions. On the other hand, the DFT-HSE band gaps are very close to the experimental values. Therefore, for charged defect calculations, DFT-HSE, when paired with PBE(+ U) or SCAN(+ U) ionic relaxation, likely offers the best compromise of speed and accuracy. However, in situations where even single-point DFT-HSE calculations are impractical, then a less accurate but far more efficient approach would be to use PBE + U with *ab initio*-derived U values [96], which predicts an acceptable band gap of 0.93 eV in CZTS and has been used to evaluate the variation of defect formation energies with the Fermi level in our previous work [66].

V. CONCLUSIONS

This work introduced and elucidated two important XC functional challenges associated with DFT modeling of CZTS and CZGS, which are relevant for photovoltaic and thermoelectric applications: (1) the systematic overbinding of Ge-containing compounds by SCAN and (2) the quantitative variability of defect thermodynamics for different combinations of XC functionals and Hubbard U corrections. The first challenge is related to SCAN's treatment of Ge and the need for XC functional and PAW potential development. The second indicated that different XC functionals predict different defect formation energies. Notably, the trends in ΔE_f^d were largely functional independent with SCAN providing lower bound estimates of defect formation energies. For this reason and due to its firm theoretical underpinning, we recommend the concurrent use and development of SCAN for modeling quaternary chalcogenides.

ACKNOWLEDGMENTS

E.A.C. thanks the U.S. Department of Energy, Office of Science, Basic Energy Sciences, under Grant No. DE-SC0002120 for funding this project. The authors thank Dr. John Mark P. Martinez and Ms. Nari L. Baughman for a careful reading of the manuscript.

- [1] H. Katagiri, K. Jimbo, W. S. Maw, K. Oishi, M. Yamazaki, H. Araki, and A. Takeuchi, *Thin Solid Films* **517**, 2455 (2009).
 [2] T. K. Todorov, K. B. Reuter, and D. B. Mitzi, *Adv. Mater.* **22**, E156 (2010).

- [3] B. Shin, O. Gunawan, Y. Zhu, N. A. Bojarczuk, S. J. Chey, and S. Guha, *Prog. Photovolt. Res. Appl.* **21**, 72 (2013).
 [4] G. Sai Gautam, T. P. Senftle, N. Alidoust, and E. A. Carter, *J. Phys. Chem. C* **122**, 27107 (2018).

- [5] A. Walsh, S. Chen, S. H. Wei, and X. G. Gong, *Adv. Energy Mater.* **2**, 400 (2012).
- [6] S. Chen and L.-W. Wang, *Chem. Mater.* **24**, 3659 (2012).
- [7] K. Iwashina, A. Iwase, Y. H. Ng, R. Amal, and A. Kudo, *J. Am. Chem. Soc.* **137**, 604 (2015).
- [8] A. Iwase, S. Yoshino, T. Takayama, Y. H. Ng, R. Amal, and A. Kudo, *J. Am. Chem. Soc.* **138**, 10260 (2016).
- [9] M. L. Liu, I. W. Chen, F. Q. Huang, and L. D. Chen, *Adv. Mater.* **21**, 3808 (2009).
- [10] J. Zhang, R. Liu, N. Cheng, Y. Zhang, J. Yang, C. Uher, X. Shi, L. Chen, and W. Zhang, *Adv. Mater.* **26**, 3848 (2014).
- [11] C. P. Heinrich, T. W. Day, W. G. Zeier, G. J. Snyder, and W. Tremel, *J. Am. Chem. Soc.* **136**, 442 (2014).
- [12] P. Hohenberg and W. Kohn, *Phys. Rev.* **136**, B864 (1964).
- [13] W. Kohn and L. J. Sham, *Phys. Rev.* **140**, A1133 (1965).
- [14] E. A. Carter, *Science* **321**, 800 (2008).
- [15] R. J. Maurer, C. Freysoldt, A. M. Reilly, J. G. Brandenburg, O. T. Hofmann, T. Björkman, S. Lebègue, and A. Tkatchenko, *Annu. Rev. Mater. Res.* **49**, 1 (2019).
- [16] K. Burke, *J. Chem. Phys.* **136**, 150901 (2012).
- [17] J. Hafner, C. Wolverton, and G. Ceder, *MRS Bull.* **31**, 659 (2006).
- [18] P. J. Hasnip, K. Refson, M. I. J. Probert, J. R. Yates, S. J. Clark, and C. J. Pickard, *Philos. Trans. R. Soc. A: Math. Phys. Eng. Sci.* **372**, 20130270 (2014).
- [19] L. J. Sham and M. Schlüter, *Phys. Rev. Lett.* **51**, 1888 (1983).
- [20] A. J. Cohen, P. Mori-Sánchez, and W. Yang, *Phys. Rev. B* **77**, 115123 (2008).
- [21] K. A. Johnson and N. W. Ashcroft, *Phys. Rev. B* **58**, 15548 (1998).
- [22] L. J. Sham and M. Schlüter, *Phys. Rev. B* **32**, 3883 (1985).
- [23] J. P. Perdew, *Int. J. Quantum Chem.* **28**, 497 (1985).
- [24] P. Mori-Sánchez, A. J. Cohen, and W. Yang, *Phys. Rev. Lett.* **100**, 146401 (2008).
- [25] D. Spagnoli, K. Refson, K. Wright, and J. D. Gale, *Phys. Rev. B* **81**, 094106 (2010).
- [26] D. A. Kitchaev, H. Peng, Y. Liu, J. Sun, J. P. Perdew, and G. Ceder, *Phys. Rev. B* **93**, 045132 (2016).
- [27] M. A. Watson, K. Hongo, T. Iitaka, and A. Aspuru-Guzik, *ACS Symp. Ser.* **1094**, 101 (2012).
- [28] J. G. Brandenburg and S. Grimme, *Acta Crystallogr. Sect. B Struct. Sci. Cryst. Eng. Mater.* **72**, 502 (2016).
- [29] J. G. Brandenburg, T. Maas, and S. Grimme, *J. Chem. Phys.* **142**, 124104 (2015).
- [30] S. Feng and T. Li, *J. Chem. Theory Comput.* **2**, 149 (2006).
- [31] C. R. Taylor, P. J. Bygrave, J. N. Hart, N. L. Allan, and F. R. Manby, *Phys. Chem. Chem. Phys.* **14**, 7739 (2012).
- [32] F. Labat, P. Baranek, C. Domain, C. Minot, and C. Adamo, *J. Chem. Phys.* **126**, 154703 (2007).
- [33] L. Wang, T. Maxisch, and G. Ceder, *Phys. Rev. B* **73**, 195107 (2006).
- [34] J. I. Martínez, H. A. Hansen, J. Rossmeisl, and J. K. Nørskov, *Phys. Rev. B* **79**, 045120 (2009).
- [35] A. Zoroddu, F. Bernardini, P. Ruggerone, and V. Fiorentini, *Phys. Rev. B* **64**, 045208 (2001).
- [36] V. Stevanović, S. Lany, X. Zhang, and A. Zunger, *Phys. Rev. B* **85**, 115104 (2012).
- [37] G. Hautier, S. P. Ong, A. Jain, C. J. Moore, and G. Ceder, *Phys. Rev. B* **85**, 155208 (2012).
- [38] V. L. Chevrier, S. P. Ong, R. Armiento, M. K. Y. Chan, and G. Ceder, *Phys. Rev. B* **82**, 075122 (2010).
- [39] F. Tran, R. Laskowski, P. Blaha, and K. Schwarz, *Phys. Rev. B* **75**, 115131 (2007).
- [40] P. Kovács, F. Tran, P. Blaha, and G. K. H. Madsen, *J. Chem. Phys.* **150**, 164119 (2019).
- [41] S. Jana, A. Patra, and P. Samal, *J. Chem. Phys.* **149**, 044120 (2018).
- [42] F. Tran, J. Stelzl, and P. Blaha, *J. Chem. Phys.* **144**, 204120 (2016).
- [43] E. Cockayne and E. B. Nelson, *J. Chem. Phys.* **143**, 024701 (2015).
- [44] P. Hao, J. Sun, B. Xiao, A. Ruzsinszky, G. I. Csonka, J. Tao, S. Glindmeyer, and J. P. Perdew, *J. Chem. Theory Comput.* **9**, 355 (2013).
- [45] J. P. Perdew, A. Ruzsinszky, J. Sun, and M. R. Pederson, Chapter one - Paradox of self-interaction correction: How can anything so right be so wrong? *Advances In Atomic, Molecular, and Optical Physics*, Vol. 64 (Elsevier, 2015), pp. 1–14.
- [46] Y. Yamamoto, C. M. Diaz, L. Basurto, K. A. Jackson, T. Baruah, and R. R. Zope, *J. Chem. Phys.* **151**, 154105 (2019).
- [47] G. Sai Gautam and E. A. Carter, *Phys. Rev. Mater.* **2**, 095401 (2018).
- [48] M. J. Lucero, T. M. Henderson, and G. E. Scuseria, *J. Phys.: Condens. Matter* **24**, 145504 (2012).
- [49] A. J. Garza and G. E. Scuseria, *J. Phys. Chem. Lett.* **7**, 4165 (2016).
- [50] W. P. Huhn and V. Blum, *Phys. Rev. Mater.* **1**, 033803 (2017).
- [51] V. I. Anisimov, J. Zaanen, and O. K. Andersen, *Phys. Rev. B* **44**, 943 (1991).
- [52] H. J. Kulik, *J. Chem. Phys.* **142**, 240901 (2015).
- [53] T. Z. H. Gani and H. J. Kulik, *J. Chem. Theory Comput.* **12**, 5931 (2016).
- [54] P. Mori-Sánchez and A. J. Cohen, *Phys. Chem. Chem. Phys.* **16**, 14378 (2014).
- [55] A. A. Emery and C. Wolverton, *Sci. Data* **4**, 170153 (2017).
- [56] B. Dorado, B. Amadon, M. Freyss, and M. Bertolus, *Phys. Rev. B* **79**, 235125 (2009).
- [57] M. Cococcioni and S. de Gironcoli, *Phys. Rev. B* **71**, 035105 (2005).
- [58] N. J. Mosey and E. A. Carter, *Phys. Rev. B* **76**, 155123 (2007).
- [59] N. J. Mosey, P. Liao, and E. A. Carter, *J. Chem. Phys.* **129**, 014103 (2008).
- [60] J. Sun, A. Ruzsinszky, and J. P. Perdew, *Phys. Rev. Lett.* **115**, 036402 (2015).
- [61] J. P. Perdew, K. Burke, and M. Ernzerhof, *Phys. Rev. Lett.* **77**, 3865 (1996).
- [62] H. Peng, Z. H. Yang, J. P. Perdew, and J. Sun, *Phys. Rev. X* **6**, 041005 (2016).
- [63] J. H. Yang, D. A. Kitchaev, and G. Ceder, *Phys. Rev. B* **100**, 035132 (2019).
- [64] E. B. Isaacs and C. Wolverton, *Phys. Rev. Mater.* **2**, 063801 (2018).
- [65] Y. Zhang, D. A. Kitchaev, J. Yang, T. Chen, S. T. Dacek, R. A. Sarmiento-Pérez, M. A. L. Marques, H. Peng, G. -Ceder, J. P. Perdew, and J. Sun, *npj Comput. Mater.* **4**, 9 (2018).
- [66] G. Sai Gautam, T. P. Senftle, and E. A. Carter, *Chem. Mater.* **30**, 4543 (2018).

- [67] S. Berman, G. Sai Gautam, and E. A. Carter, *ACS Sustain. Chem. Eng.* **7**, 5792 (2019).
- [68] S. Hadke, S. Levchenko, G. Sai Gautam, C. J. Hages, J. A. Márquez, V. Izquierdo-Roca, E. A. Carter, T. Unold, and L. H. Wong, *Adv. Energy Mater.* **9**, 1902509 (2019).
- [69] O. Y. Long, G. Sai Gautam, and E. A. Carter, *Phys. Rev. Mater.* **4**, 045401 (2020).
- [70] A. Khare, B. Himmetoglu, M. Cococcioni, and E. S. Aydil, *J. Appl. Phys.* **111**, 123704 (2012).
- [71] W. G. Zeier, H. Zhu, Z. M. Gibbs, G. Ceder, W. Tremel, and G. J. Snyder, *J. Mater. Chem. C* **2**, 10189 (2014).
- [72] W. Xiao, J. N. Wang, X. S. Zhao, J. W. Wang, G. J. Huang, L. Cheng, L. J. Jiang, and L. G. Wang, *Solar Energy* **116**, 125 (2015).
- [73] D. Huang and C. Persson, *Thin Solid Films* **535**, 265 (2013).
- [74] K. Yu and E. A. Carter, *Chem. Mater.* **27**, 2920 (2015).
- [75] K. Yu and E. A. Carter, *Chem. Mater.* **28**, 4415 (2016).
- [76] K. Yu and E. A. Carter, *Chem. Mater.* **28**, 864 (2016).
- [77] J. Paier, R. Asahi, A. Nagoya, and G. Kresse, *Phys. Rev. B* **79**, 115126 (2009).
- [78] S. Botti, D. Kammerlander, and M. A. L. Marques, *Appl. Phys. Lett.* **98**, 241915 (2011).
- [79] S. Kim, J. S. Park, and A. Walsh, *ACS Energy Lett.* **3**, 496 (2018).
- [80] K. Tse, M. Wong, Y. Zhang, J. Zhang, M. Scarpulla, and J. Zhu, *J. Appl. Phys.* **124**, 165701 (2018).
- [81] S. Chen, X. G. Gong, A. Walsh, and S. H. Wei, *Appl. Phys. Lett.* **96**, 021902 (2010).
- [82] S. Chen, J. H. Yang, X. G. Gong, A. Walsh, and S. H. Wei, *Phys. Rev. B* **81**, 245204 (2010).
- [83] L. Hedin, *Phys. Rev.* **139**, A796 (1965).
- [84] F. Aryasetiawan and O. Gunnarsson, *Reports Prog. Phys.* **61**, 237 (1998).
- [85] W. G. Aulbur, L. Jönsson, and J. W. Wilkins, *Solid State Phys.* **54**, 1 (2000).
- [86] M. S. Hybertsen and S. G. Louie, *Phys. Rev. Lett.* **55**, 1418 (1985).
- [87] M. S. Hybertsen and S. G. Louie, *Phys. Rev. B* **34**, 5390 (1986).
- [88] A. V. Krukau, O. A. Vydrov, A. F. Izmaylov, and G. E. Scuseria, *J. Chem. Phys.* **125**, 224106 (2006).
- [89] D. H. Seo, A. Urban, and G. Ceder, *Phys. Rev. B* **92**, 115118 (2015).
- [90] N. W. Ashcroft and N. D. Mermin, *Solid State Physics* (Holt, Rinehart, and Winston, New York, 1976).
- [91] G. Kresse and J. Hafner, *Phys. Rev. B* **47**, 558 (1993).
- [92] G. Kresse and J. Hafner, *Phys. Rev. B* **49**, 14251 (1994).
- [93] G. Kresse and J. Furthmüller, *Phys. Rev. B* **54**, 11169 (1996).
- [94] G. Kresse and D. Joubert, *Phys. Rev. B* **59**, 1758 (1999).
- [95] S. L. Dudarev, G. A. Botton, S. Y. Savrasov, C. J. Humphreys, and A. P. Sutton, *Phys. Rev. B* **57**, 1505 (1998).
- [96] K. Yu and E. A. Carter, *J. Chem. Phys.* **140**, 121105 (2014).
- [97] P. E. Blöchl, *Phys. Rev. B* **50**, 17953 (1994).
- [98] A. Jain, S. P. Ong, G. Hautier, W. Chen, W. D. Richards, S. Dacek, S. Cholia, D. Gunter, D. Skinner, G. Ceder, and K. A. Persson, *APL Mater.* **1**, 011002 (2013).
- [99] See Supplemental Material at <http://link.aps.org/supplemental/10.1103/PhysRevB.102.054101> for further details about planewave and k -point convergence tests, PAW datasets, theoretical and experimental formation enthalpies and lattice constants, theoretical chemical potentials and a sample calculation of them for the constrained Cu-poor condition, interactions between periodic images of the same defect, crystal structures of the nonkesterite polymorphs and kesterite defect configurations of Cu_2ZnXS_4 where X is either Sn or Ge, and XC functional dependence of defect formation energies and polymorph preference in Cu_2ZnXS_4 .
- [100] *Thermodynamic Properties of Inorganic Substances*, edited by I. Hurtado, D. Neuschütz, and P. Franke (Springer, Berlin, 1973).
- [101] *Non-Tetrahedrally Bonded Elements and Binary Compounds I*, edited by O. Madelung, U. Rössler, and M. Schulz (Springer-Verlag, Berlin, 1998).
- [102] G. Kim, S. V. Meschel, P. Nash, and W. Chen, *Sci. Data* **4**, 170162 (2017).
- [103] B. Brunetti, V. Piacente, and P. Scardala, *J. Alloys Compd.* **206**, 113 (1994).
- [104] *Thermodynamic Properties of Inorganic Materials Compiled by SGTE, Subvolume C: Ternary Steel Systems, Phase Diagrams and Phase Transition Data, Part 2: Ternary Systems from Cr-Mn-N to Ni-Si-Ti*, 1st ed., edited by A. Watson and T. Markus, Vol. 19C2 (Springer-Verlag, Berlin, Heidelberg, 2019).
- [105] D. Broberg, B. Medasani, N. E. R. Zimmermann, G. Yu, A. Canning, M. Haranczyk, M. Asta, and G. Hautier, *Comput. Phys. Commun.* **226**, 165 (2018).
- [106] C. Freysoldt, B. Grabowski, T. Hickel, J. Neugebauer, G. Kresse, A. Janotti, and C. G. Van de Walle, *Rev. Mod. Phys.* **86**, 253 (2014).
- [107] M. Malitckaya, H.-P. Komsa, V. Havu, and M. J. Puska, *Adv. Electron. Mater.* **3**, 1600353 (2017).
- [108] W. Setyawan and S. Curtarolo, *Comput. Mater. Sci.* **49**, 299 (2010).
- [109] S. P. Ong, W. D. Richards, A. Jain, G. Hautier, M. Kocher, S. Cholia, D. Gunter, V. L. Chevrier, K. A. Persson, and G. Ceder, *Comput. Mater. Sci.* **68**, 314 (2013).
- [110] O. Kubaschewski and C. B. Alcock, *Metallurgical Thermochemistry*, 5th ed. (Pergamon Press, Oxford, England, 1959).
- [111] I. Barin, *Thermochemical Data of Pure Substances* (Wiley, Weinheim, Germany, 1995).
- [112] D. D. Wagman, W. H. Evans, V. B. Parker, R. H. Schumm, I. Halow, S. M. Bailey, K. L. Churney, and R. L. Nuttall, *J. Res. Natl. Inst. Stan.* **125**, 125007 (2020).
- [113] S. Grimme, *J. Comput. Chem.* **27**, 1787 (2006).
- [114] A. Janotti and C. G. Van de Walle, *Rep. Prog. Phys.* **72**, 126501 (2009).
- [115] S. B. Zhang, S.-H. Wei, and A. Zunger, *Phys. Rev. B* **63**, 075205 (2001).
- [116] S. Chen, A. Walsh, X.-G. Gong, and S.-H. Wei, *Adv. Mater.* **25**, 1522 (2013).
- [117] S. Lany and A. Zunger, *Phys. Rev. B* **78**, 235104 (2008).
- [118] C. Freysoldt, J. Neugebauer, and C. G. Van de Walle, *Phys. Rev. Lett.* **102**, 016402 (2009).
- [119] S. Chen, L. W. Wang, A. Walsh, X. G. Gong, and S. H. Wei, *Appl. Phys. Lett.* **101**, 223901 (2012).
- [120] Y. S. Yee, B. Magyari-Köpe, Y. Nishi, S. F. Bent, and B. M. Clemens, *Phys. Rev. B* **92**, 195201 (2015).

- [121] Z. Xu, Z. Guan, J. Yang, and Q. Li, *ACS Appl. Energy Mater.* **2**, 2779 (2019).
- [122] F. A. Kröger and H. J. Vink, *Solid State Phys.* **3**, 307 (1956).
- [123] J. A. Brehm, H. Takenaka, C. W. Lee, I. Grinberg, J. W. Bennett, M. R. Schoenberg, and A. M. Rappe, *Phys. Rev. B* **89**, 195202 (2014).
- [124] S. Kirklin, J. E. Saal, B. Meredig, A. Thompson, J. W. Doak, M. Aykol, S. Rühl, and C. Wolverton, *npj Comput. Mater.* **1**, 15010 (2015).
- [125] R. G. Hennig, A. Wadehra, K. P. Driver, W. D. Parker, C. J. Umrigar, and J. W. Wilkins, *Phys. Rev. B* **82**, 014101 (2010).
- [126] D. Mejía-Rodríguez and S. B. Trickey, *Phys. Rev. B* **100**, 041113(R) (2019).
- [127] G. L. Agawane, S. A. Vanalakar, A. S. Kamble, A. V. Moholkar, and J. H. Kim, *Mater. Sci. Semicond. Process.* **76**, 50 (2018).
- [128] H. Guo, Y. Li, X. Guo, N. Yuan, and J. Ding, *Phys. B: Condens. Matter* **531**, 9 (2018).
- [129] J. Kim, H. Hiroi, T. K. Todorov, O. Gunawan, M. Kuwahara, T. Gokmen, D. Nair, M. Hopstaken, B. Shin, Y. S. Lee, W. Wang, H. Sugimoto, and D. B. Mitzi, *Adv. Mater.* **26**, 7427 (2014).
- [130] B. G. Janesko, T. M. Henderson, and G. E. Scuseria, *Phys. Chem. Chem. Phys.* **11**, 443 (2009).
- [131] T. M. Henderson, J. Paier, and G. E. Scuseria, *Phys. Status Solidi Basic Res.* **248**, 767 (2011).
- [132] Z. H. Yang, H. Peng, J. Sun, and J. P. Perdew, *Phys. Rev. B* **93**, 205205 (2016).
- [133] J. P. Perdew, W. Yang, K. Burke, Z. Yang, E. K. U. Gross, M. Scheffler, G. E. Scuseria, T. M. Henderson, I. Y. Zhang, A. Ruzsinszky, H. Peng, J. Sun, E. Trushin, and A. Görling, *Proc. Natl. Acad. Sci. USA* **114**, 2801 (2017).
- [134] Y. Zhang, X. Sun, P. Zhang, X. Yuan, F. Huang, and W. Zhang, *J. Appl. Phys.* **111**, 063709 (2012).
- [135] S. Delbos, *EPJ Photovoltaics* **3**, 35004 (2012).
- [136] M. Kumar, A. Dubey, N. Adhikari, S. Venkatesan, and Q. Qiao, *Energy Environ. Sci.* **8**, 3134 (2015).
- [137] A. Nagoya, R. Asahi, R. Wahl, and G. Kresse, *Phys. Rev. B* **81**, 113202 (2010).
- [138] A. Walsh, S. Chen, X. G. Gong, and S.-H. Wei, in *Physics of Semiconductors: 30th International Conference on the Physics of Semiconductors*, edited by J. Ihm and H. Cheong, AIP Conf. Proc. No. 1399 (AIP, New York, 2011), p. 63.
- [139] M. J. Romero, H. Du, G. Teeter, Y. Yan, and M. M. Al-Jassim, *Phys. Rev. B* **84**, 165324 (2011).
- [140] J. Sun, R. C. Remsing, Y. Zhang, Z. Sun, A. Ruzsinszky, H. Peng, Z. Yang, A. Paul, U. Waghmare, X. Wu, M. L. Klein, and J. P. Perdew, *Nat. Chem.* **8**, 831 (2016).